H. Moodley, S. Afshan, D. Crump, M.M. Kashani. (2024) Testing and numerical modelling of circular stainless steel reinforced concrete columns. Engineering Structures. 304, 117607.

Testing and numerical modelling of circular stainless steel reinforced concrete columns.

H. Moodley*, S. Afshan, D. Crump, M.M. Kashani

Faculty of Engineering and Physical Sciences, University of Southampton, UK

* Corresponding author Email: h.t.m.moodley@soton.ac.uk

Abstract

Chloride-induced corrosion of carbon steel reinforcing bars is considered the primary cause of deterioration of reinforced concrete (RC) structures. Stainless steel rebars have gained increasing attention in recent years as a promising alternative to the traditional carbon steel rebars to overcome the problem of chloride-induced reinforcement corrosion in RC structures. This paper presents the results of a new experimental testing program on two circular RC columns, subjected to lateral cyclic loading, reinforced with two different stainless steel reinforcing bar grades: austenitic EN 1.4301 and duplex EN 1.4362. A third RC column reinforced with carbon steel reinforcing bar was tested as a control specimen. The resultant force-displacement relationships, damage, energy dissipation, secant stiffness, and moment-curvature relationships from digital image correlation (DIC) are presented and discussed. Finally, an advanced OpenSees finite element model, validated against the conducted tests, for simulating the cyclic response of RC columns is presented.

Keywords: Circular column, Cyclic loading, Experimentation, Stainless steel, Reinforcing bar, OpenSees modelling

1. Introduction

Reinforced concrete (RC) has been and remains extensively used in the construction of bridges worldwide. However, RC bridges are prone to various forms of deterioration of both concrete and steel reinforcing bars (rebar) as a consequence of their age, heavy use, and also climate and environmental factors. This is particularly important for RC bridges located in high-chloride concentration environments, such as in coastal regions and in areas where de-icing salts are applied during winter. The presence of chloride causes the initiation and propagation of chloride-induced rebar corrosion, which is considered the most common cause of premature deterioration in reinforced concrete structures. As a result, regular maintenance becomes

necessary which carries significant financial and environmental implications. Sustaining the functionality and minimising the social, economic and environmental impacts of aging reinforced concrete bridge infrastructure is of high priority in developed countries. In the UK £750 million is spent annually [1] on repairing damaged concrete construction, while Western Europe allocates €5 billion per year [2]. The US spends $8 billion per year [3] on bridge maintenance. These direct costs are relatively easier to quantify compared to the extensive social and economic impacts that arise from the loss of service experienced by the population. Several durability measures are currently implemented in practice to control the corrosion of steel reinforcement, primarily through a combination of the concrete mix quality, concrete cover thickness and crack width control [4–6]. However, the desirable high alkali environment provided by the designed concrete mix is not always maintained during the service life of RC structures due to the inherent nature of concrete as a deteriorating porous material [4,7]. Increasing the cover thickness also increases the potential for cracking due to tensile stress, shrinkage and thermal effects [4,7]. Therefore, while these measures reduce the rate of chloride diffusion, and hence delay the corrosion initiation time, they do not permanently eliminate reinforcement corrosion over the entire service life of the structure. To address the aforementioned issues related to rebar corrosion, the use of alternative corrosion-resistant reinforcement solutions, such as stainless steel rebar, basalt rebar, galvanised rebar, epoxy-coated rebar and fibre-reinforced polymer (FRP) rebars, have gained increased popularity in recent years. Ongoing research studies to characterise their structural behaviour are progressively being carried out as reported in the literature e.g. [8–10].

This paper focuses on the use of stainless steel rebars in bridge piers. In highway bridges, columns (piers) are typically situated in central reserves and/or abutments, which means their end regions may experience a higher rate of corrosion due to the proximity to the road and presence of water carrying chloride from the deck expansion joints. Therefore, employing stainless steel rebar in these structural elements can effectively eliminate the corrosion problem. While the initial material cost of stainless steel rebar is higher than that of carbon steel, several life cycle cost (LCC) and life cycle assessment (LCA) studies have demonstrated that over the required service life of a structure, stainless steel provides RC designs with reduced economic costs and environmental impact compared with carbon steel RC designs [11]. The behaviour and design of RC structures with stainless steel rebar has been the topic of several recent experimental and numerical modelling research studies, full reviews of which have been reported by several review papers such as those by Rabi et al. [12], Yuan et al. [13]

and Moodley et al. [14]. There remains limited literature in the public domain on the structural behaviour of stainless steel RC columns subjected to lateral cyclic loading [15–17].

This paper presents the results of a large-scale laboratory test programme on circular reinforced concrete cantilever columns. Three specimens, one reinforced with austenitic EN 1.4301 stainless steel rebars, another reinforced with duplex EN 1.4362 stainless steel rebars, and a control specimen reinforced with carbon steel B500 rebars were tested. The details of the tests and the measured test responses, including the force-displacement relationships, moment-curvature responses, secant stiffnesses and dissipated hysteretic energy are described and discussed. Furthermore, advanced finite element (FE) models of the columns were developed using the open-source platform OpenSees [18] and were validated against the conducted tests. The development of the FE models and the validation results are also presented.

2. Experimental investigation

A laboratory testing programme was carried out in the Large Structures Testing Laboratory (LSTL) at the University of Southampton to investigate the structural performance of circular reinforced concrete columns with stainless steel reinforcing bars under cyclic lateral loading. Three columns were tested: two were reinforced with austenitic EN 1.4301 and duplex EN 1.4362 stainless steel rebars, while one was reinforced with B500 carbon steel rebar, which served as the control specimen. The details of the material tests conducted to measure the mechanical properties of the reinforcing bars and concrete, as well as the column tests are described hereafter.

2.1. Material tests

All tested columns contained 8 mm and 16 mm diameter rebars as transverse and longitudinal reinforcements, respectively. Tensile tests were performed in accordance with EN ISO 6892-1 [19] to determine the tensile stress-strain behaviour of the rebars using the same setup as described in [20], the results of which are presented in **Figure 1**. A total of three repeat tests were performed on the 16 mm stainless steel rebars, while two repeat tests were performed on all other rebars. The mean values of the key measured mechanical properties of the cold-rolled (CR) and hot-rolled (HR) rebars are presented in **Table 1**, where E is the Young's modulus, $f_{0.2}$ is the yield strength taken as the 0.2% proof stress, f_u is the ultimate tensile strength, ε_u is the strain at the ultimate tensile stress and ε_f is the strain at fracture. The parameters n and n'_u of the two-stage Ramberg-Osgood material model were also determined according to the method described in Afshan et al. [21] and their values are reported in **Table 1**. The concrete mix design

per m^3 consisted of 420 kg of high-strength cement, 901 kg of 4 – 10mm stone (flint), 823 kg of 0 – 4mm sand, 1.8 litres of admix and 160 litres of water. The compressive cube strength of the concrete used in the columns was measured at 28 days after casting in accordance with EN 12390-3:2019 [22]. The measured mean 28 day compressive cube strengths were 65.2 MPa, 64.9 MPa and 75.4 MPa for the austenitic stainless steel, duplex stainless steel and carbon steel reinforced concrete columns, respectively.

2.2. Column Specimens

The columns were designed following the requirements of Eurocode 2 [23] and Eurocode 8 [24]. They all had the same dimensions and reinforcement detailing as illustrated in **Figure 2.** The cross-section of each column had a diameter of 0.4 m, and the overall height of the column was 2 m including an additional 0.4 m long 0.5 m × 0.5 m square section at the top of the column to facilitate the application of the lateral cyclic loading from the actuator. The longitudinal reinforcement consisted of a total of nine 16 mm diameter rebars. The transverse reinforcement bars were 8 mm in diameter and were spaced vertically at 80 mm intervals, resulting in a hoop spacing to longitudinal rebar diameter ratio (L/D) of 5, which is within the Eurocode 8 recommended L/D ≤ 6 [24]. The clear concrete cover was 30 mm in all columns. The columns were cast into a rigid foundation block with dimensions of 1.5 m ×1.5 m × 0.4 m, which was fixed to the LSTL strong floor using pre-tensioned steel rods to prevent slippage or overturning of the specimen during testing.

2.3. Test set-up and instrumentation

The column tests were conducted in a purpose-built test rig that was constructed in the LSTL laboratory for performing lateral cyclic loading on large-scale structural components. The adopted test set-up, as shown in **Figure 3**, involved a horizontal 250 kN capacity Instron actuator with a ±125 mm stroke for applying the lateral cyclic load. No axial load was applied to the columns. The actuator was connected to a reaction frame, which, like the column, was rigidly fixed to the strong floor of the laboratory using pre-tensioned steel rods to prevent slippage of the frame during testing. Lateral displacement was applied at the mid-height of the square section at the top of the column, giving the columns an effective height of 1.8 m, through a displacement-controlled loading scheme, as depicted in **Figure 4**. The following lateral displacements were applied in the tests: 1.6, 2.25, 2.8, 3.5, 4.4, 5.5, 6.9, 8, 10.7, 13.4, 16, 24, 32, 40, 48, 56, 64, 72, 80, 88 and 96 mm. The adopted loading protocol consisted of two repeated cycles for each lateral deformation level, following the recommendations of ACI 374.2R-13 [25].

The measurement instrumentation included 5 linear variable differential transducers (LVDTs) to measure the displacement of the column at different height points. Digital Image Correlation (DIC) was employed, in accordance with [26], to capture the full-field strain in the plastic hinge region of the columns. DIC is an imaging technique which allows non-contact measurement of strain and displacements in structures during deformation. It involves taking a reference image of the region of interest on the column specimen when it is in the unloaded state, before structural deformations occur, followed by continuously capturing further images as the column experiences deformations, which are known as the deformed images. The deformed images are then compared with the reference image to compute the displacements and strains in the region of interest. A random speckle pattern was applied to the specimen, which was divided into a number of subsets. The deformation of each subset was used to correlate the displacements and strains of the plastic hinge region of the column. As the columns had a circular geometry with a curved surface, stereo DIC consisting of a pair of two cameras for both areas of interest were employed. DIC strain fields were obtained, from the captured images, using MatchID Stereo software. The adopted DIC set-up and the speckle pattern employed are shown in **Figure 5**. Furthermore, the cameras, settings and parameters used in DIC are presented in **Table 2**.

3. Experimental results and discussion

3.1. Force – displacement

The measured lateral force-displacement response curves of the austenitic EN 1.4301 and duplex EN 1.4362 stainless steel and B500 carbon steel reinforced concrete columns are presented in **Figure 6**. Both the full cyclic response and the cyclic envelope curves are shown in **Figures 6(a)** and **6(b)**, respectively. The figures are presented with a double x-axis, representing the column displacement in mm on the bottom axis and % lateral drift on the top axis. Drift is calculated as the percentage of the lateral displacement divided by 1.8 m which is the height of the column, taken from the foundation block to the middle of the actuator. The peak loads attained in both the positive and the negative loading directions are also shown in **Figure 6(a)** with dashed lines.

The key response characteristics of the tested columns including the maximum force $F_{c,max}$, drift at maximum force $\delta_{c,max}$, yield drift δ_y, ultimate force $F_{c,ult}$, drift at ultimate force $\delta_{c,ult}$ and displacement ductility $\mu_{\Delta,ult}$, corresponding to the positive and negative loading directions, are presented in **Tables 3** and **4,** respectively. The ultimate point is typically taken as the point at

which there is a strength reduction of 20% relative to the maximum force as adopted in [27] and other similar studies [[17], [28]]. This definition was adopted for the carbon steel column ultimate point. However, since the cyclic loading was ended before this drop in strength was observed for the stainless steel columns, the ultimate point for these columns was defined as the load at the maximum applied drift point. The displacement ductility at the ultimate point was computed as the ratio of the drift at the ultimate force $\delta_{c,ult}$ and the yield drift δ_y. The yield drift δ_y is based on the yield displacement d^*_y determined from the energy equivalent area method described in Eurocode 8-1 [29] as given by **Eq. (1)**, where, d^*_m is the displacement at maximum force (mm), E^*_m is the area under the force-displacement curve up to maximum force (kNmm), and F^*_y is the maximum force (kN). A schematic of these parameters is shown in **Figure 7**.

$$d_y^* = 2\left(d_m^* - \frac{E_m^*}{F_y^*}\right) \quad (1)$$

As shown in **Figure 6(b)**, all columns demonstrate similar force-displacement responses up to about 0.5% drift, beyond which the behaviour of the carbon steel column and the stainless steel columns differ. The carbon steel column reaches its maximum force at a drift value of 2.2% in both the positive and negative loading directions. In comparison, the austenitic and duplex stainless steel columns reach their maximum forces at larger drifts, with the austenitic stainless steel column having a higher drift at maximum force than the duplex stainless steel column, as reported in **Tables 3** and **4**. This is attributed to the comparatively higher strength and ductility of the longitudinal stainless steel reinforcing bars compared to their carbon steel counterpart – see **Table 1**. The maximum force of the carbon steel and duplex stainless steel columns in both loading directions were similar, as they both exhibited similar yield strengths, 539 MPa and 530 MPa, respectively. However, the maximum strength of the austenitic stainless steel column was greater than the duplex stainless steel and carbon steel columns, particularly in the positive loading direction.

Following the maximum force, the carbon steel column exhibited a gradual softening response until 3% and 4% drift in the positive loading direction and the negative loading direction, respectively. Beyond these drifts, the carbon steel column experienced a more pronounced drop in force towards the ultimate point where the longitudinal reinforcing bars began to fracture, in the positive loading direction – see **Figure 6(a)**. The response of the stainless steel columns post maximum force exhibited comparatively less softening than the carbon steel column and no rebar fracture was observed within the applied maximum drifts. The pinching behaviour of

all columns was similar. The observed asymmetry of the force-displacement behaviour in the positive and negative loading directions of the columns (**Figure 6**) can be attributed to potential asymmetry in the longitudinal reinforcement layout. The yield drift values, obtained from the energy equivalent area method, for the stainless steel columns are higher than that of the carbon steel column, which is primarily due to the greater drift values of these columns at maximum force. In terms of the displacement ductility, although the stainless steel values presented in **Tables 3** and **4** show comparable results to the carbon steel columns. Overall, the global cyclic performance of the stainless steel columns, predominantly the austenitic stainless steel column, was superior to that of the carbon steel column, due to the stainless steels' higher strength and ductility, which is in agreement with previous literature [17].

3.2. Observed damage

The first visible flexural cracks appeared on the carbon steel column at 1.33% drift, while those on the stainless steel columns appeared at greater lateral drifts, 2.67% and 2.22% for the austenitic and duplex stainless steel columns, respectively. Initiation of spalling of the concrete cover occurred at about 2.67% drift for both the carbon steel and austenitic stainless steel columns and at a higher drift of 3.11% for the duplex stainless steel column. While the carbon steel column exhibited significant buckling of the longitudinal reinforcing bars, which was first observed at about 4% drift, the stainless steel columns did not visibly demonstrate the same levels of bar buckling. The carbon steel column showed rebar fracture at 4.88% and 5.33% drifts during the unloading-reloading from compression to tension stage, which was caused by the combined effects of inelastic bar buckling and low-cycle fatigue [30] as also observed in previous tests on carbon steel RC columns ([31], [32]). The final failure of the carbon steel column was due to inelastic buckling and low-cycle fatigue. The stainless steel columns did not reach final failure under the applied loading protocol. The observed damage states of the columns, at the end of each test, are shown **Figure 8**. All columns demonstrated splitting between the column base and the foundation, indicating reinforcing bar slip and strain penetration at the base of the columns [33]. Comparisons of the observed damage at the end of the test shows that the spalling of the concrete cover is significantly greater in the carbon steel column compared with the stainless steel columns (**Figure 8**). The plastic hinge length of each column was recorded at the end of test, as the spalled concrete length, and were 270 mm, 220 mm and 210 mm for the carbon steel, austenitic stainless steel, and duplex stainless steel columns, respectively. However, at the end of test, there were a greater number of cracks in the

stainless steel columns than the carbon steel column, which is due to the presence of potentially higher degree of bar slippage in the these columns [34], the higher ductility of stainless steel rebars resulting in a greater distribution of strain in the rebar, and the lower concrete strength of the stainless steel RC columns.

3.3. Energy dissipation

The progression of the accumulated hysteretic dissipated energy with increasing drift of the columns is presented in **Figure 9**. Dissipated energy (kNm) is calculated as the sum of the interior area of the force-displacement cycles at each drift ratio. The hysteretic dissipated energy of all columns was similar up to 1.33% drift. Beyond 1.33% drift, the carbon steel column had a steeper increase in dissipated energy, due to the greater levels of damage experienced, reaching a total hysteretic dissipated energy of 31.51 kNm at the adopted ultimate point. The dissipated hysteretic energy of the two stainless steel columns remained broadly similar to one another up to about 4% drift, beyond which, the austenitic stainless steel column started to dissipate a marginally higher amount of energy at each drift ratio. The total dissipated energy corresponding to the ultimate load point of the austenitic and duplex stainless steel columns were 81.44 kNm and 76.81 kNm, respectively, which correspond to 158% and 144% increase of that of the carbon steel column (31.51 kNm). It is important to note that if the tests had continued beyond the maximum applied drifts, the stainless steel columns, with their greater residual capacity, would have been able to reach their conventional, 20% drop in maximum strength, ultimate load point and therefore demonstrated an even greater energy dissipation capacity. The greater total hysteretic dissipated energy of the stainless steel columns in comparison with the carbon steel column is evidence of the superior ductility, in terms of both the ultimate and fracture strains and the ultimate-to-yield strength ratio of the material, and is in agreement with the findings for rectangular RC columns from Melo et al. [17]

3.4. Effective secant stiffness

The effective mean secant stiffness of the force-displacement responses of the columns at each drift level were determined and are compared in **Figure 10.** The secant stiffness K_{sec} (kN/mm) was computed using **Eq. (2)**, where $F^{+/-}_{max,i}$ is the peak force in the positive (+) or negative (-) loading direction in kN and $\delta^{+/-}_{max,i}$ is the corresponding peak displacement in the positive (+) or negative (-) loading direction in mm for each loop. The austenitic stainless steel reinforced column demonstrated similar initial stiffness to the carbon steel reinforced column up to about 1.33% drift, beyond which, the stiffness of the carbon steel reinforced column degraded at a greater rate, as it experienced larger damage in the plastic hinge zone. The initial stiffness of

the duplex stainless steel reinforced column was lower than that of the other two tested columns, but at higher drifts, above 2.2%, the stiffness of the carbon steel reinforced column started to drop below that of the duplex stainless steel column. At the greatest applied drift values, the stiffness of the austenitic stainless steel reinforced column is marginally higher than that of the duplex stainless steel and carbon steel reinforced columns, which is due to its comparatively higher strain-hardening.

$$K_{sec} = \frac{\left|F^{+}_{max,i}\right| + \left|F^{-}_{max,i}\right|}{\left|\delta^{+}_{max,i}\right| + \left|\delta^{-}_{max,i}\right|} \quad (2)$$

3.5. Digital Image Correlation (DIC) results

Figure 11 presents a selection of the DIC strain fields for each of the tested columns. The strain fields depict the von Mises equivalent strain at three specific points: (i) at the cracking moment, (ii) at the predicted yield drift δ_y and (iii) at the drift corresponding to the maximum force $\delta_{c,ult}$. Based on the DIC results, the first flexural cracks in both the austenitic stainless steel and carbon steel columns were observed after the first lateral cycles at a drift of 0.09%, as shown in **Figures 11(a)** and **11(g)**, respectively. In contrast, the duplex stainless steel column exhibited the first flexural cracks at a higher drift of 0.16%, as depicted in **Figure 11(d)**. It is important to note that the first flexural cracks detected by the DIC occurred at significantly lower drift values compared to the first visibly observed flexural cracks in all the tested columns. At both the yield drift and the drift corresponding to the maximum force, the number of flexural cracks and the magnitude of the crack widths increased in all the tested columns. The stainless steel columns exhibited a higher number of cracks compared to the carbon steel column. This can be attributed to the potentially weaker bond [[35], [36]], as the other main parameters influencing crack spacing, i.e. bar diameter-to-effective reinforcement ratio and concrete cover, were constant in all columns [37]. Further research is needed to investigate the bond strength of stainless steel rebars and its impact on crack spacing and crack widths in RC structures.

The maximum tensile and compressive strains corresponding to the two extreme fibres of the cross-section within the plastic hinge zone regions of the columns were extracted from the DIC measurements. The plastic hinge length was taken as L_p = 400 mm. The extreme fibre strains were taken as the average strain over the central 100 mm wide by 200 mm height portion of the plastic hinge length. The extreme fibre strains were used to calculate the curvature k_z (1/mm) at the column plastic hinge based on the Euler-Bernoulli beam theory, as given **Eq. (3)**, where $\varepsilon_{max,t}$ and $\varepsilon_{max,c}$ are the extreme fiber strains on the tension and compression faces relative

to the loading direction of the column, respectively and d is the column depth (mm). A schematic of these parameters is shown in **Figure 12**.

$$k_z = \frac{\varepsilon_{max,t} - \varepsilon_{max,c}}{d} \quad (3)$$

Figure 13 shows the derived moment-curvature responses up to 2.22% drift, which is the drift at the maximum strength of the carbon steel column. In the positive loading direction, the cracking moment of the duplex stainless steel column was higher than that of the other two tested columns. Beyond the cracking moment, the duplex stainless steel shows a similar response to the carbon steel column as the curvature increases in the positive loading direction, while the austenitic stainless steel column exhibits a higher moment. In the negative loading direction, all columns presented similar cracking moments. However, in contrast to the moment-curvature response in the positive loading direction, the moment of the carbon steel column is greater than that of the stainless steel columns at the same curvature, which could be due to asymmetric distribution of the longitudinal reinforcing bars in the columns.

4. Numerical modelling

This section presents the development and validation results of numerical models for the three tested circular RC columns. The calibrated models will be used in future numerical parametric studies involving stainless steel reinforced concrete columns with different geometries, rebar configurations and axial load conditions.

4.1. Model development

The numerical models were developed in the open-source finite element analysis software OpenSees (Open System for Earthquake Engineering Simulation) [18]. The columns were modelled using the nonlinear force-based distributed plasticity beam-column element *forceBeamColumn* available in OpenSees. Fibre sections were assigned to the column cross-section at distinct locations known as integration points. Individual steel and concrete fibres were defined to characterise the reinforcing steel, the unconfined concrete (cover) and the confined concrete (core). The Gauss-Lobatto integration scheme, which allows the definition of integration points at the column base and distributed along the length of the column, was adopted. Four integration points, including one at the column base, were defined as recommended by Du et al. [38]. The fibre section mesh consisted of 20 fibres in both the radial and the circumferential directions for the core concrete. In the cover concrete, it comprised of 1 fibre in the radial direction and 20 fibres in the circumferential direction, based on the recommendations by Berry and Eberhard [39]. The measured geometry and rebar configuration

of the tested specimens were used in the numerical models. Rotational and displacement boundary conditions were applied at the ends of the columns to replicate the experimental conditions. At the base, all degrees of freedom (DOF) were restrained, while at the loaded end, all DOFs were set free. **Figure 14** presents a schematic representation of the column models.

The stress-strain responses of the unconfined concrete, confined concrete and steel reinforcing bars were modelled using the *Concrete02*, *Concrete04* and *Hysteretic* material models available in the OpenSees material library, respectively. The material parameters used in the Concrete02 and Concrete04 models are presented in **Table 5**, where f_c is the maximum compressive strength, ε_0 is the strain at the maximum compressive strength, ε_{cu} is the strain at crushing strength and f_{tu} is the tensile strength. The compressive strength of the unconfined concrete was taken as the 28 day cylinder strength estimated from the measured cube strength using the cubic-to-cylindrical strength ratio of 0.8 [40]. The confined concrete model proposed by Mander et al. [41] was used to estimate the material parameters for the confined concrete, as presented in **Table 5**.

The trilinear *Hysteretic* material model was used to represent the stress-strain response of the reinforcing bars. The key model parameters are reported in **Table 6** and their calibration is described hereafter. The model was fitted to the measured monotonic tensile stress-strain response of the reinforcing bars and the best fit stress and strain values for the first (σ_1, ε_1), second (σ_2, ε_2) and third (σ_3, ε_3) points of the tensile envelope were determined. The unloading stiffness of the hysteretic response is controlled by the unloading rule proposed by Takeda et al. [42] through the β_{mu} parameter. For the carbon steel column model the default value of the $\beta_{mu} = 0.4$ was used. The pinching factors for the strain and stress during the reloading stage i.e. pinching X and pinching Y parameters, respectively were taken as those recommended in [43] for the carbon steel column. The unloading stiffness β_{mu} and the pinching X and Y parameters of the stainless steel column models were calibrated against the column tests. The use of the damage parameters, available in the hysteretic model, was also investigated for modelling the reduction in the peak stress at large strain demands. The damage parameter, Damage1, which models strength reductions proportional to the strain level, was adopted. For the carbon steel column, the Damage1 parameter was calibrated against the force degradation in the negative loading direction of the experimental force-displacement response, as fracture did not occur in this loading direction, and an ad hoc value of 0.008 was deemed appropriate for this particular test. For the stainless steel columns, no damage was included in the models. The models assumed perfect bond conditions and no strain penetration effects were included. The

experimental lateral loading protocol was applied to the column models at the unrestrained node and their lateral force-displacement response was recorded.

4.2. Numerical model results

The numerical and experimental force-displacement response curves for the austenitic stainless steel, duplex stainless steel and carbon steel (excluding damage1) columns are shown in **Figures 15**, **16** and **17**, respectively. The numerical force-displacement of the carbon steel column including damage1 is presented in **Figure 18**. It is shown that the numerical models can accurately replicate the overall cyclic lateral force-displacement responses of the columns. A comparison between the numerical and experimental peak forces and lateral drift at the maximum force is presented in **Table 7**. In the positive loading direction, the numerically predicted peak forces were in good agreement with the experimental values, while in the negative loading direction they were slightly under-predicted. This under-prediction is due to the potential asymmetric distribution of the steel reinforcing bars around the cross-section of the columns. In all the numerical models, the peak force occurred at a lower drift value than the corresponding experimental. This discrepancy between the numerical and experimental results can be attributed to the perfect bond conditions assumed in the numerical models, hence neglecting the impact of strain penetration from slip. The inclusion of the damage1 parameter in the carbon steel column (**Figure 18**), compared to the carbon steel model excluding damage1 (**Figure 17**), presents a better prediction of the post-peak force degradation. The hysteretic energy dissipation evolution of the numerical and experimental results is compared in **Figure 19**. The dissipated energy evolution was taken as the sum of the energy dissipation associated to each loading cycle, and corresponded to the interior area of the force-displacement loops. All the numerical models dissipate a lower amount of energy than the experimental results at drift values below 1%. At larger drifts, the numerical carbon steel models with and without damage1 shows good agreement with the experimental results up to 3% drift. Beyond 3% drift, the numerical model with damage 1 shows lower dissipated energy than that observed from the experiments, which is due to the larger damage experienced by the tested column at the larger drift demand cycles. For both the stainless steel reinforced columns, the numerical models had a lower dissipated energy up to about 4% drift, beyond which the numerical models show good agreement with their experimental counterparts.

5. Conclusion

The high corrosion resistance of stainless steel rebars, compared with carbon steel, makes it a promising solution to reduce the economic and carbon costs of repair and replacement of RC structures due to rebar corrosion. However, to fully optimise the design of stainless steel RC structures and to realise its full potential cost savings, the behaviour of stainless steel RC structural elements under a range of loading conditions needs to be comprehensively understood. This paper experimentally investigated the lateral cyclic performance of two circular RC columns reinforced with two different grades of stainless steel rebar: austenitic EN 1.4301 and duplex EN 1.4362. A third RC column reinforced with carbon steel rebar was also tested as a control specimen. Furthermore, numerical models of the tested columns were developed, and validated against the experimental results. The main conclusions of the study are summarised as follows:

- The yield drift and drift at maximum force of the stainless steel columns were notably greater than the carbon steel column. The maximum lateral force capacity of the austenitic stainless steel column was greater than the duplex stainless steel and carbon steel columns, which had similar maximum force capacities. The stainless steel columns demonstrated a lesser degree of post maximum force softening than the carbon steel column. Overall, the use of stainless steel rebars, particularly the austenitic stainless steel, was demonstrated to improve the lateral cyclic performance of circular RC columns.
- The observed damage at the end of tests demonstrated a greater degree of concrete spalling in the carbon steel column in comparison to the stainless steel columns. Furthermore, the carbon steel column experienced fracture of longitudinal rebars, due to inelastic buckling and low-cycle fatigue. At the end of tests, the plastic hinge lengths of the stainless steel columns were smaller than the carbon steel column, which can be attributed to the greater amount of reinforcing bar slip in the stainless steel columns.
- The austenitic and duplex stainless steel columns dissipated 158% and 144% more hysteretic energy at the ultimate point than the carbon steel column, respectively. Therefore, highlighting the improved cyclic performance of stainless steel RC columns and their suitability for use in seismic regions.
- Under small lateral drift (< 1%) the secant stiffness of the austenitic stainless steel and carbon steel columns were similar. The duplex stainless steel column had a lower initial

secant stiffness than the other tested columns. As drift increased, the secant stiffness of the carbon steel column degraded to a greater degree than the stainless steel columns.

- DIC was used in this study for crack detection and to measure the curvature of the columns. It was revealed from the DIC strain fields that flexural cracking, in all columns, occurred at significantly smaller drift values than the first visible cracks. The curvature was used to plot the moment-curvature relationship of the tested RC columns.
- The OpenSees results showed good agreement with the experimental force-displacement relationships. The validation results demonstrated the suitability of the developed models for simulating the response of stainless and carbon steel circular RC columns subjected to cyclic loading. Such models form the basis for future parametric and reliability studies, to inform the next generation of design guidance of stainless steel RC structural elements. Future research should calibrate uniaxial material models, such as *Hysteretic* and *ReinforcingSteel*, for B500 carbon steel and stainless steel rebars based on experimental rebar testing for implementation into RC column models, similar to the study by [28].

Acknowledgements

The authors thank Network Rail for their professional and financial support of this research. Furthermore, the authors acknowledge the support received by the UK Engineering and Physical Sciences Research Council (EPSRC) for funding the experimental programme under the grant number EP/R039178/1. The experiments were conducted in the Large Structures Testing Laboratory (LSTL), which is part of the UKCRIC National Infrastructure Laboratory (NIL), based at the University of Southampton. The help of Andrew Morgan, LSTL Technician, in setting-up the experiment is gratefully acknowledged.

References

[1] Glass GK, Buenfeld NR. Chloride-induced corrosion of steel in concrete. Prog Struct Eng Mater 2000;vol. 2(4):448–58.

[2] G. Markeset, S. Rostam, and O. Klinghoffer, "Guide for the use of stainless steel reinforcement in concrete structures," Norwegion Building Research Institute, Oslo, 2006.

[3] Koch G.H., Brongers M.P.H., Thompson N.G., Virmani Y.P., Payer J.H.“Corrosion cost and preventive strategies in the United States.,” Report No. FHWA-RD-01-156, R315-01, 2002.

[4] Tang SW, Yao Y, Andrade C, Li ZJ. Recent durability studies on concrete structure. Cem Concr Res 2015;vol. 78:143–54.

[5] Nossoni G, Harichandran RS. Electrochemical-mechanistic model for concrete cover cracking due to corrosion initiated by chloride diffusion. J Mater Civ Eng 2014;vol. 26(6).

[6] S¨ oylev TA, Özturan T. Durability, physical and mechanical properties of fiber-reinforced concretes at low-volume fraction. Constr Build Mater 2014;vol. 73: 67–75.

[7] Li Z. Advanced Concrete technology. Hoboken: John WIley & Sons; 2011.

[8] L. Salh, "Analysis and Behaviour of Structural Concrete Reinforced with Sustainable Materials," Master in Philosophy, School of Engineering, University of Liverpool, 2014. [Online]. Available:〈https://livrepository.liverpool.ac.uk/16333/4/SalhLuna_Feb2014_16333.pdf〉.

[9] Mills C, Dymond BZ. Tensile bond strength of post-installed epoxy-coated reinforcing bars. J Bridge Eng 2021;vol. 26(2):06020002.]

[10] Marek A. The impact of galvanizing on the mechanical properties of rebars. Metalurgija 2023;vol. 62(2):282–4 ([Online]. Available), 〈https://hrcak.srce.hr/290113〉.

[11] Moodley H., Blainey S., Preston J., Afshan S.Can stainless steel reinforcement bar facilitate more sustainable railway bridges? A review of life cycle cost and carbon analysis," presented at the World Congress on Railway Research.2022, Birmingham, United Kingdom 2022;06:2022.

[12] Rabi M, Shamass R, Cashell KA. Structural performance of stainless steel reinforced concrete members: a review. Constr Build Mater 2022;vol. 325.

[13] Yuan J, Ou Z. Research progress and engineering applications of stainless steel-reinforced concrete structures. Adv Civ Eng 2021;2021.

[14] H. Moodley, S. Afshan, S. Blainey, and J. Preston, "State-of-the-art review on the structural behavior of stainless steel reinforced concrete elements," in 11th International Conference on Bridge Maintenance, Safety and Management, Barcelona, 2022.

[15] Franchi A, Crespi P, Bennani A, Farinet M. Stainless steel rebar for seismic applications. " Adv Eng Strucutres, Mech Constr 2006:255–64.

[16] Fu J, Ge X, Li J, Sun Z, Wang D. Seismic performance of concrete bridge piers reinforced by stainless steel bars: a quasi-static experimental study. Eng Strucutres 2022;vol. 266.

[17] Melo J, Afshan S, Rossetto T, Varum Y, Arˆ ede A. Experimental and numerical investigation of the cyclic response of stainless steel reinforced concrete columns.

Eng Struct 2021;vol. 252.

[18] Mazzoni S, McKenna F, Scott MH, Fenves GL, et al. "OpenSees command language manual,". Pacific Earthquake Engineering Research Center. Berkeley, United States: University of California; 2007.

[19] EN ISO 6892–2016 . Metallic materials. Tensile testing. Method of test at room temperature., CEN, Brussels, Belgium, 2016.

[20] Limbert J, Afshan S, Kashani MM, Robinson AF. Compressive stress–strain behaviour of stainless steel reinforcing bars with the effect of inelastic buckling. Eng Struct 2021;vol. 237.

[21] Afshan S, Rossi B, Gardner L. Strength enhancements in cold-formed structural sections - Part I: Material testing. J Constr Steel Res 2013;vol. 83:177–88.
[22] BS EN 12390–3: 2019. Testing Hardened Concrete. Compressive Strength of Test Specimens, CEN, London, 2019.

[23] EN 1992–2 Eurocode 2: Desing of concrete structures - Part 2: Concrete bridges, CEN, 2005.

[24] EN 1998–2 Eurocode 8: Design provisions of structures for earthquake resistance - Part 2: bridges, CEN, 2005.

[25] ACI 374.2R-13 , ACI, Farmington Hills, 2013.

[26] Jones EM, Iadicola MA. "A good practices guide for digital image correlation," International Digital Image Correlation. Society 2018;vol. 10:308–12.

[27] Park R, Priestly MJN, Gill WD. Ductility of square-confined concrete columns. J Struct Eng 1982;vol. 108:929–50.

[28] Ding Y, Wu D, Su J, Li Z-X, Zong L, Feng K. Experimental and numerical investigations on seismic performance of RC bridge piers considering buckling and low-cycle fatigue of high-strength steel bars. Eng Struct 2021;vol. 227:111464. https://doi.org/10.1016/j.engstruct.2020.111464.

[29] EN 1998–1 Eurocode 8: Design of structures for earthquake resistance - Part 1: General rules, seismic actions and rules for buildings, CEN, 2004.

[30] Kashani MM, Alagheband P, Khan R, Davis S. Impact of corrosion on low-cycle fatigue degradation of reinforcing bars with the effect of inelastic buckling. Int J Fatigue 2015;vol. 77:174–85.

[31] El-Bahy A, Kunnath S, Stone W, Taylor A. Cumulative seismic damage of circular bridge columns: Variable amplitude tests. Acids Struct J 1999;vol. 96(5):711–9.

[32] Lehman D, Moehle J, Mahin S, Calderone A, Henry L. Experimental evaluation of the seismic performance of reinforced concrete bridge columns. J Struct Eng 2004; vol. 130(6):869–79.

[33] Arani KK, Marefat MS, Amrollahi-Biucky A, Khanmohammadi M. Experimental seismic evaluation of old concrete columns reinforced by plain bars. Struct Des Tall Spec Build 2013;vol. 22(3):267–90.

[34] Melo J, Varum H, Rossetto T. Experimental cyclic behaviour of RC columns with plain bars and proposal for Eurocode 8 formula improvement. Eng Struct 2015;vol. 88:22–36.

[35] Rabi M, Cashell KA, Shamass R, Desnerck P. Bond behaviour of austenitic stainless steel reinforced concrete. Eng Struct 2020;vol. 221.

[36] Freitas E, Louro AS, Costa H, Cavaco ES, Júlio E, Pipa M. Bond behaviour between steel / stainless-steel reinforcing bars and low binder concrete (lbc). Eng Struct 2020;vol. 221.

[37] EN 1992–1-1 Eurocode 2: Design of concrete structures - Part 1–1: General rules and rules for buildings., CEN, 2004.

[38] K. Du, J. Sun, and W. Xu, "Evaluation of Section and Fiber Integration Points in Fiber Model," in 15th World Conference on Earthquake Engineering, Lisbon, 2012: Curran Associates, Inc, pp. 9789–9795.

[39] Berry MP, Eberhard MO. Performance modeling strategies for modern reinforced concrete bridge. Berkeley: University of California; 2008.

[40] Pacheco JN, De Brito J, Chastre C, Evangelista L. Probabilistic conversion of the compressive strength of cubes to cylinders of natural and recycled aggregate concrete specimens (no) Materials 2019;12(2):280.

[41] Mander JB, Priestley MJN, Park R. Theoretical stress-strain model for confined concrete. J Struct Eng 1988;vol. 114(8):1804–26.

[42] T. Takeda, M.A. Sozen, and N.N. Nielsen, "Reinforced Concrete Response to Simulated Earthquakes," Journal of the Structural Division, vol. 96, no. 12, pp. 2557–2573, 1970.

[43] Kashani MM, Lowes LN, Crewe AJ, Alexander NA. Nonlinear fibre element modelling of RC bridge piers considering inelastic buckling of reinforcement. Eng Struct 2016;vol. 116:163–77.

Figures

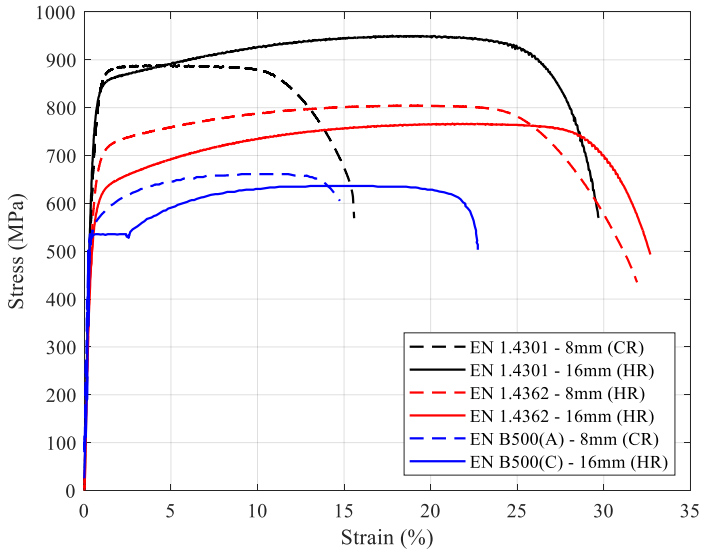

Figure 1: Measured tensile stress–strain curves of 8 mm and 16 mm diameter EN 1.4301 austenitic stainless steel, EN 1.4362 duplex stainless steel and EN B500 carbon steel

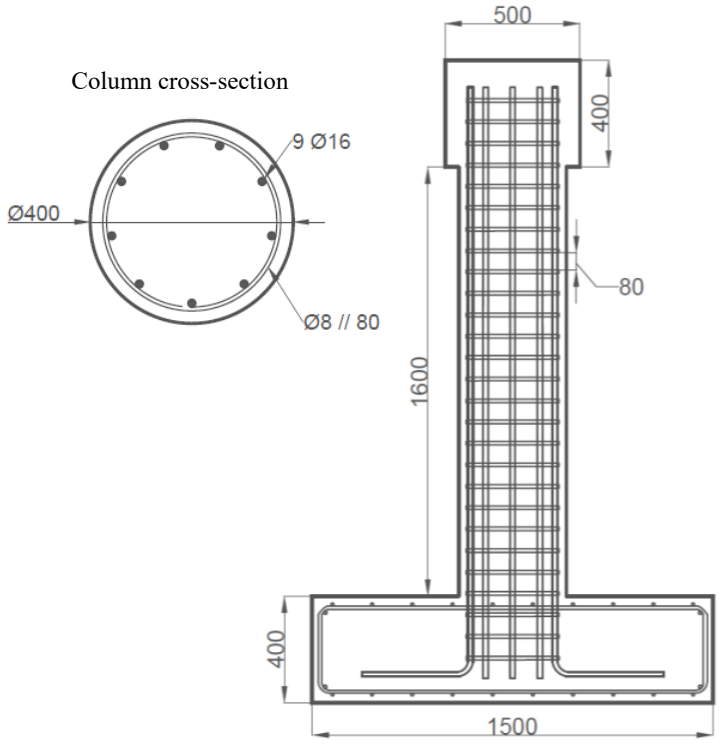

Figure 2: Dimensions (in mm) and reinforcement detailing of the tested columns.

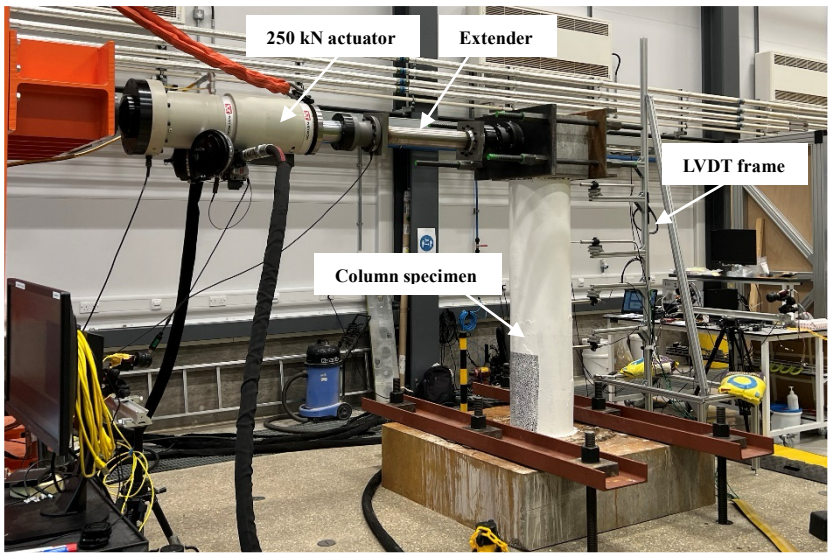

(a) Column test set-up.

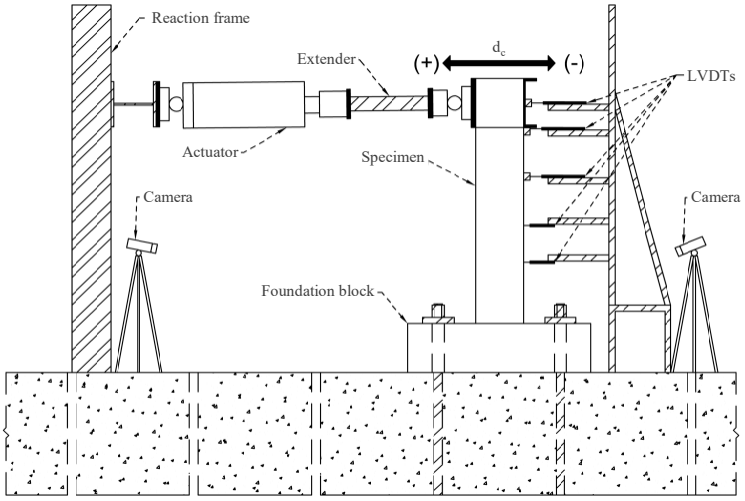

(b) Set-up schematic and measurement arrangement.

Figure 3: Arrangement of the column tests.

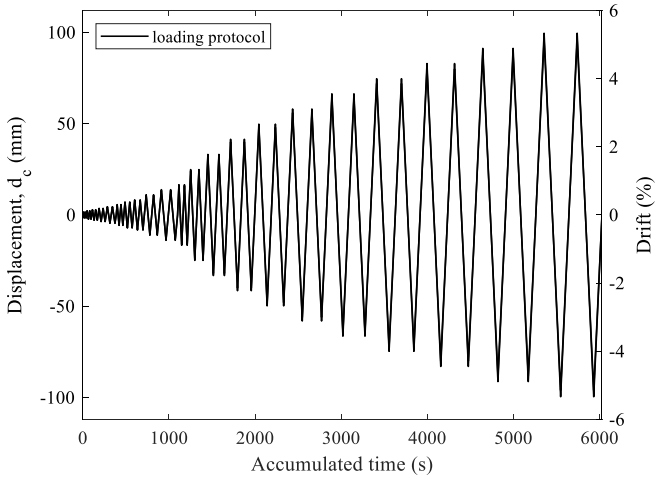

Figure 4: Column lateral loading protocol.

(a) Stereo DIC on positive displacement

(b) Stereo DIC on negative displacement

(c) DIC speckle pattern at the plastic hinge region.

Figure 5: DIC set-up: Stereo DIC configuration and applied speckle pattern.

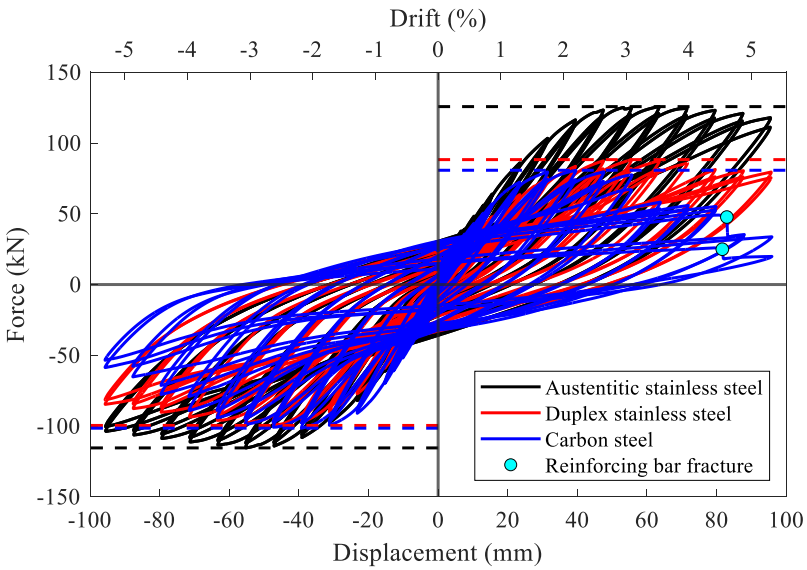

(a) Full cyclic force-displacement response curves.

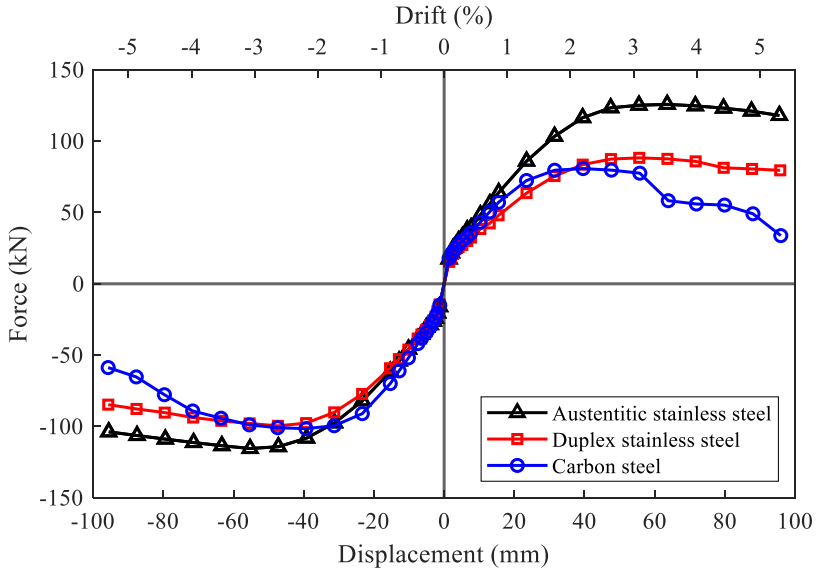

(b) Skeleton force-displacement curves.

Figure 6: Measured force-displacement response curves of the stainless and carbon steel

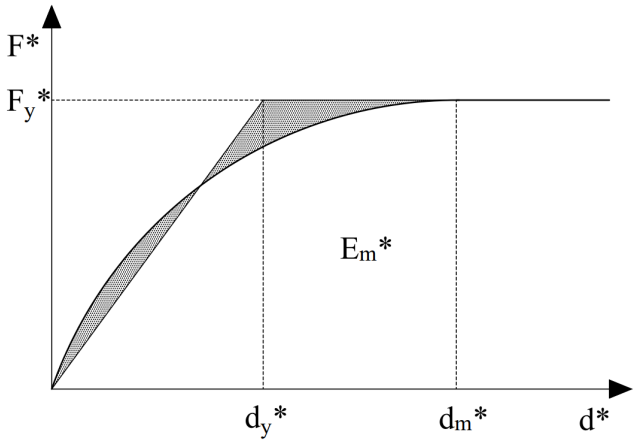

Figure 7: Schematic of parameters from the energy equivalent area method described in Eurocode 8-1-1 [24].

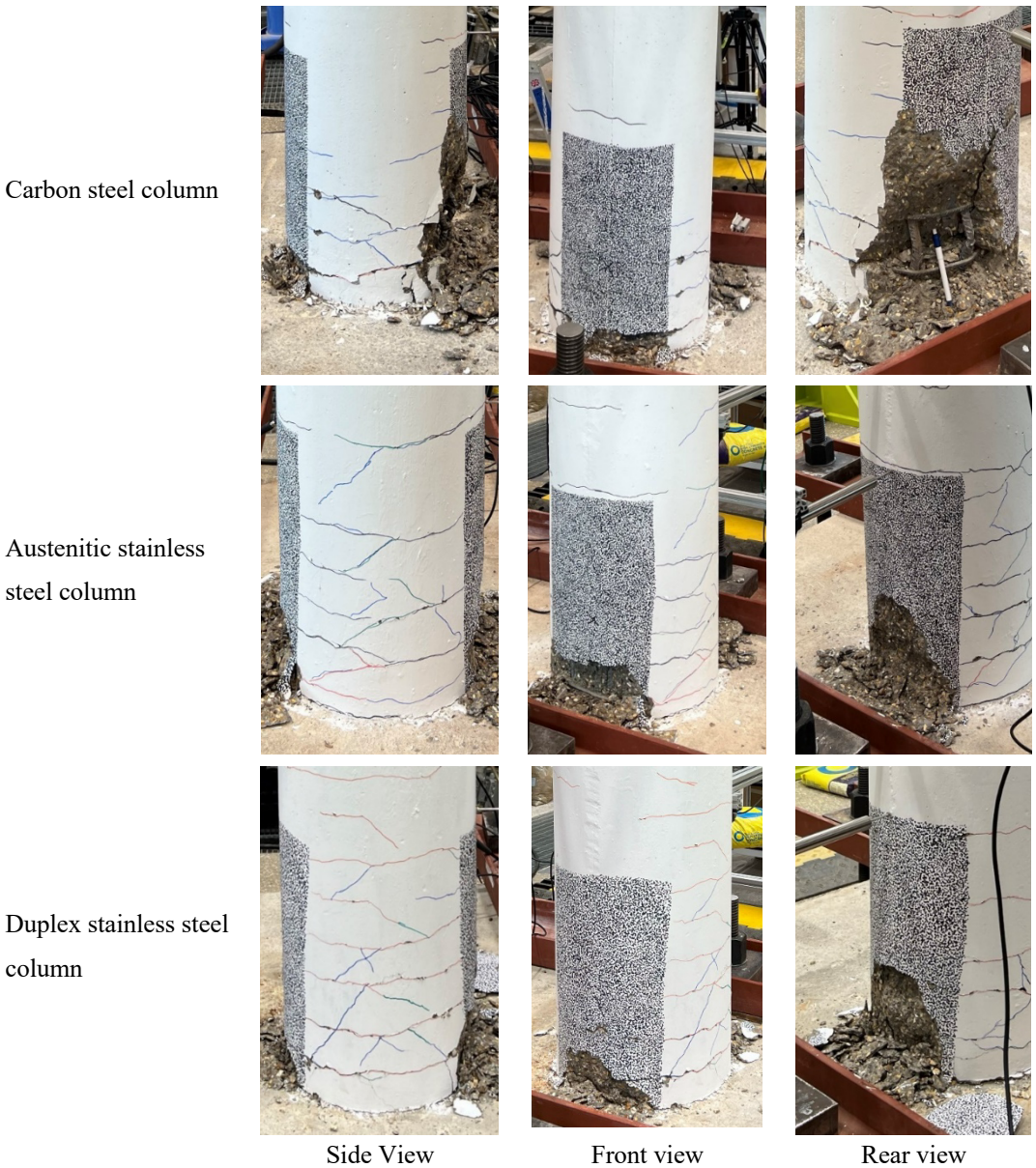

Figure 8: Damage observed at the end of test.

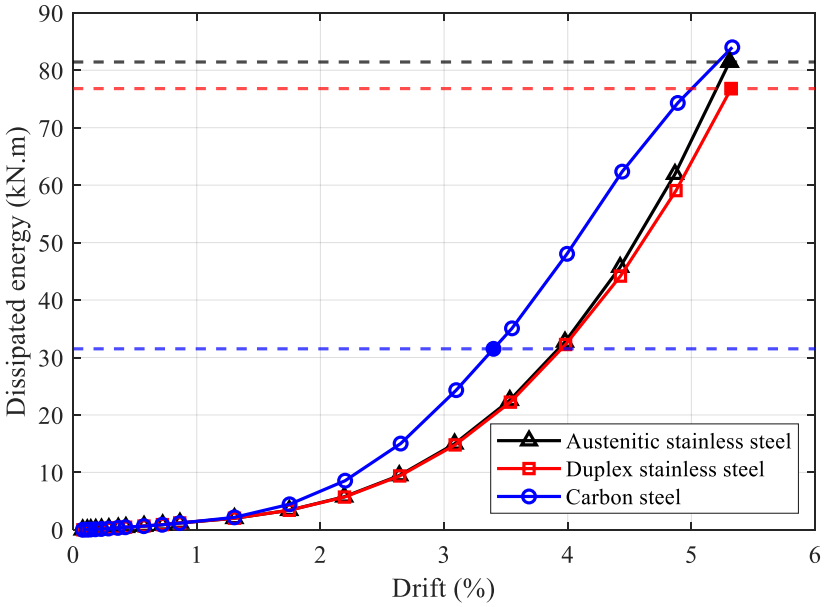

Figure 9: Total hysteretic dissipated energy

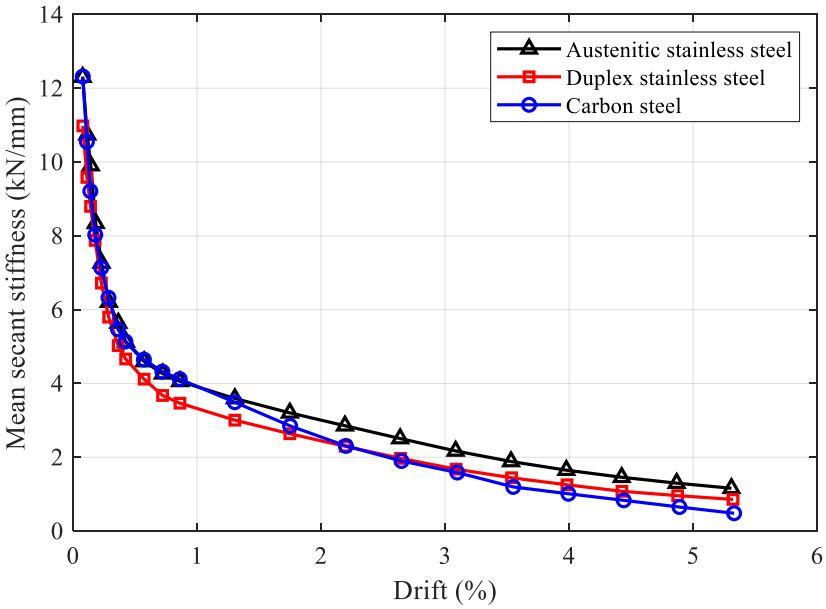

Figure 10: Comparison of the effective secant stiffness variation with increasing drift.

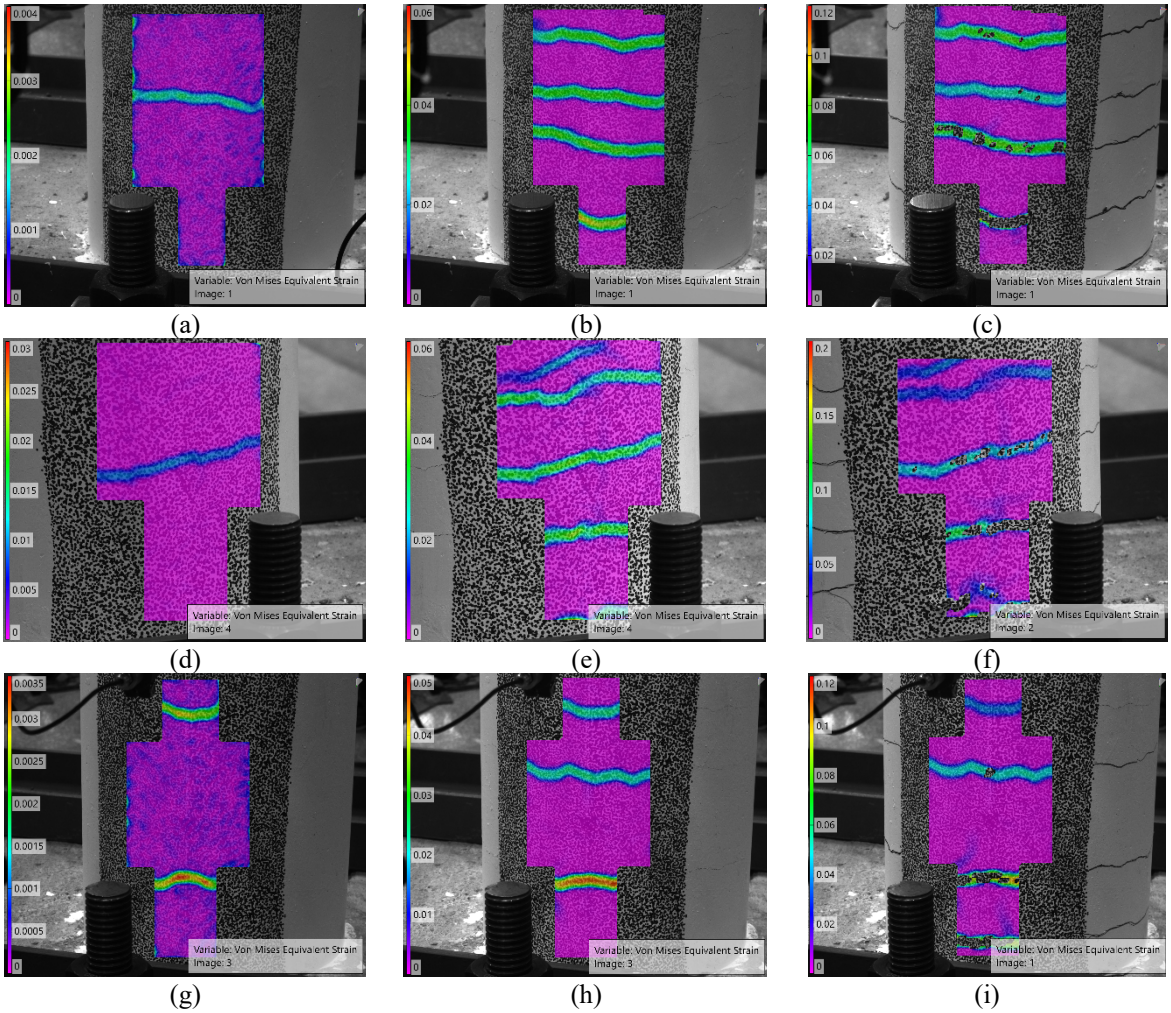

Figure 11: DIC von Mises equivalent strain fields at: the cracking moment, the predicted yield drift and the drift corresponding to the maximum force of the columns reinforced with austenitic stainless steel (a), (b) and (c), duplex stainless steel (d), (e) and (f) and carbon steel (g), (h) and (i).

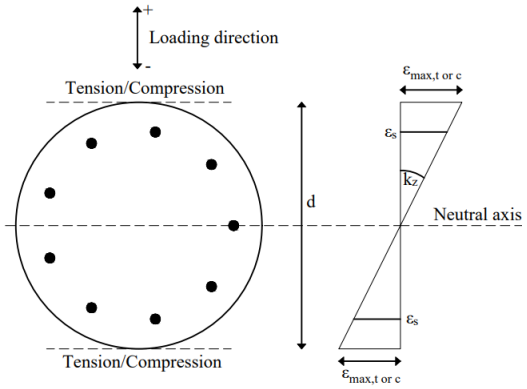

Figure 12: Strain relationship of RC column schematic

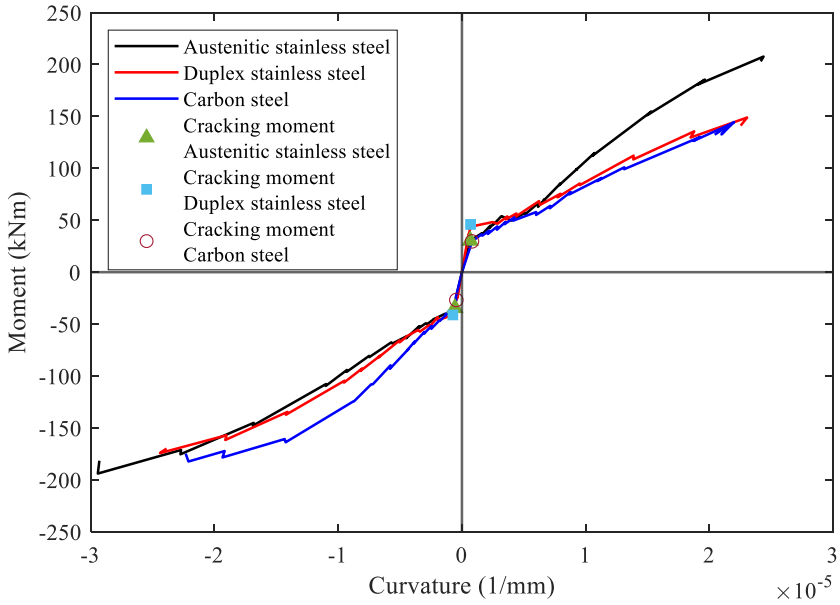

Figure 13: Moment-curvature responses of the columns reinforced with austenitic stainless steel, duplex stainless steel and carbon steel up to 2.22% drift.

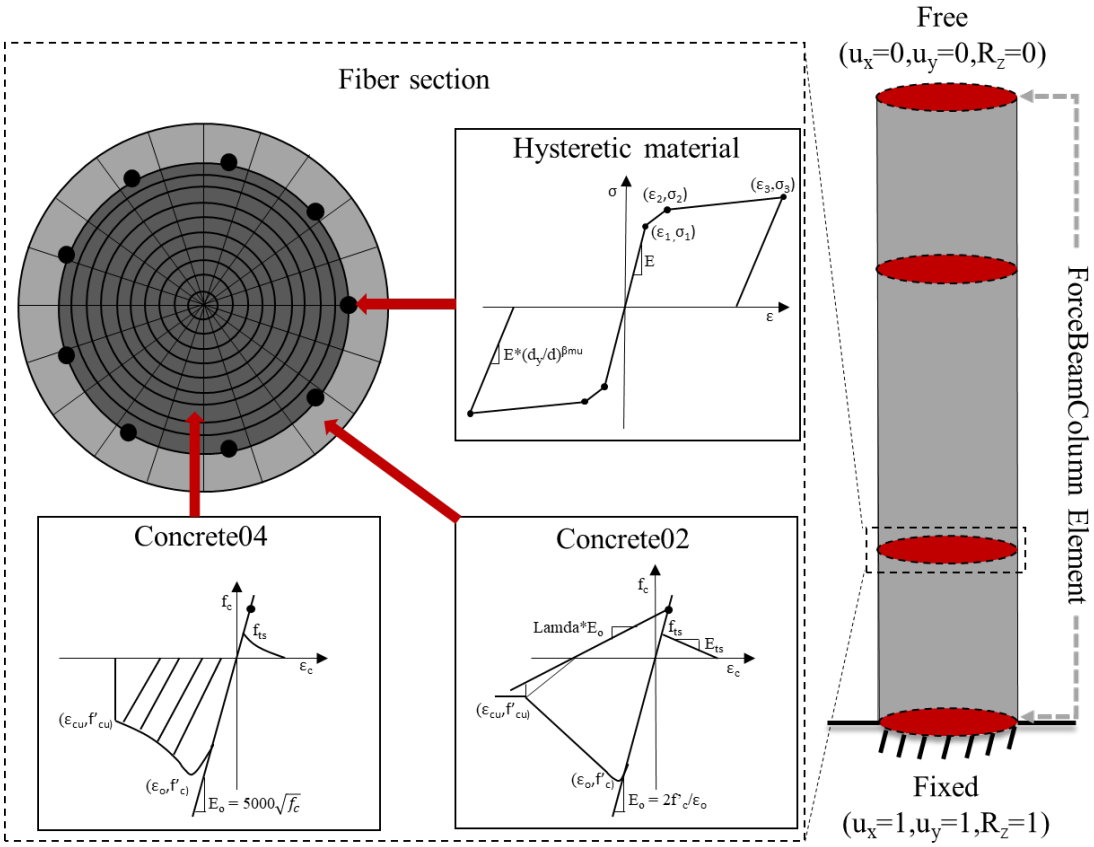

Figure 14: Schematic of the fiber section and the material models of the modelled columns.

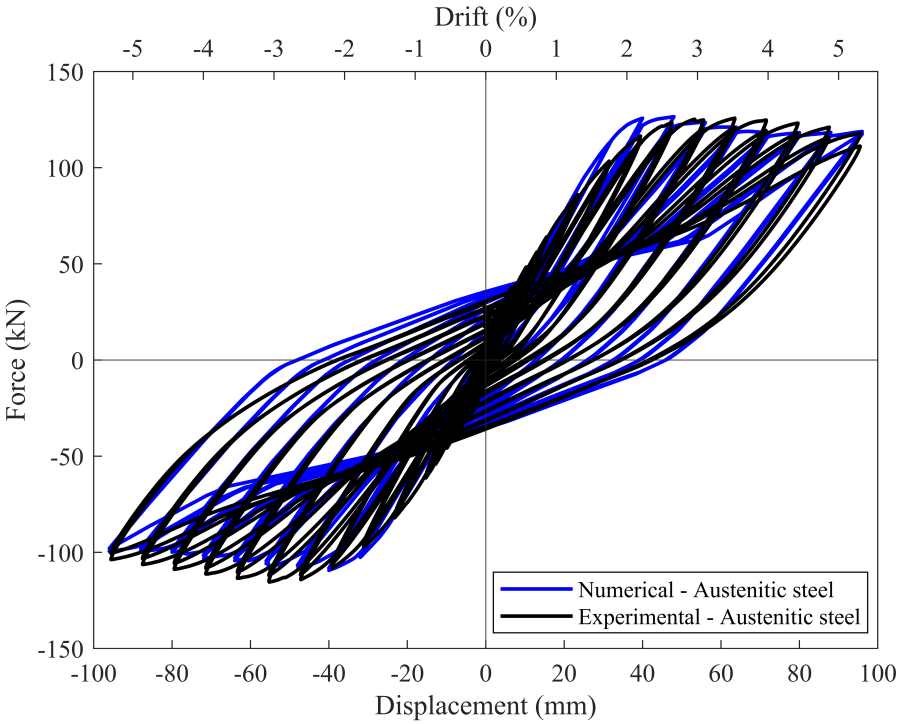

Figure 15: Numerical and experimental lateral force-drift comparisons for austenitic stainless steel column.

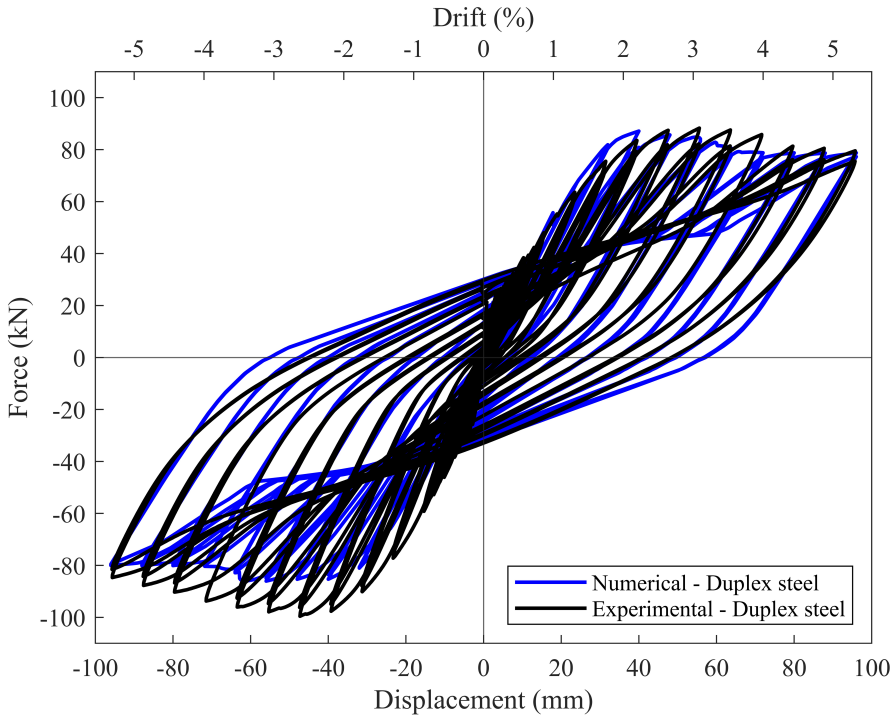

Figure 16: Numerical and experimental lateral force-drift comparisons for duplex stainless steel column.

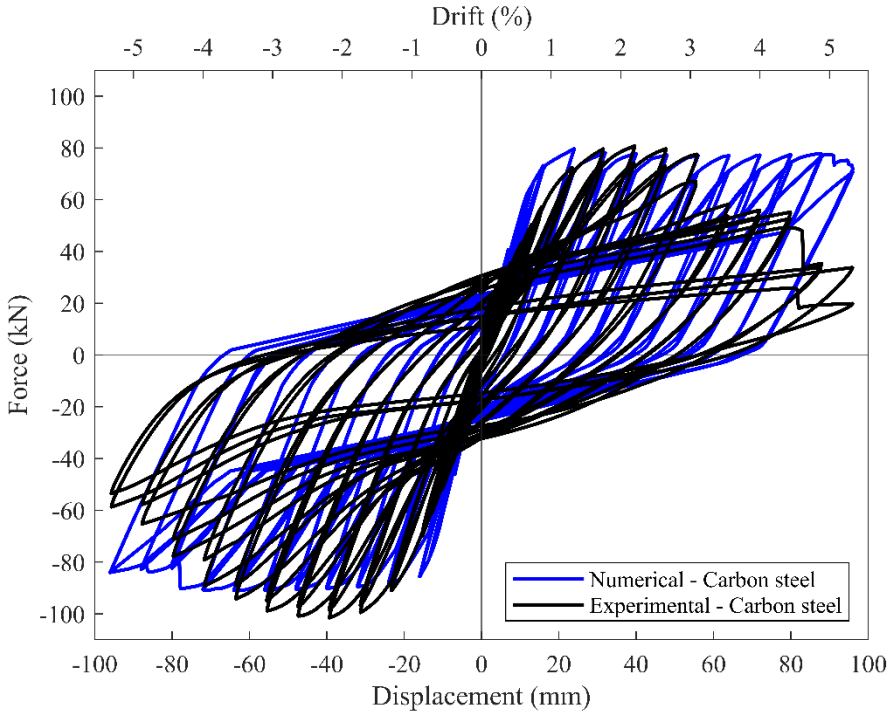

Figure 17: Numerical and experimental lateral force-drift comparison for carbon steel column.

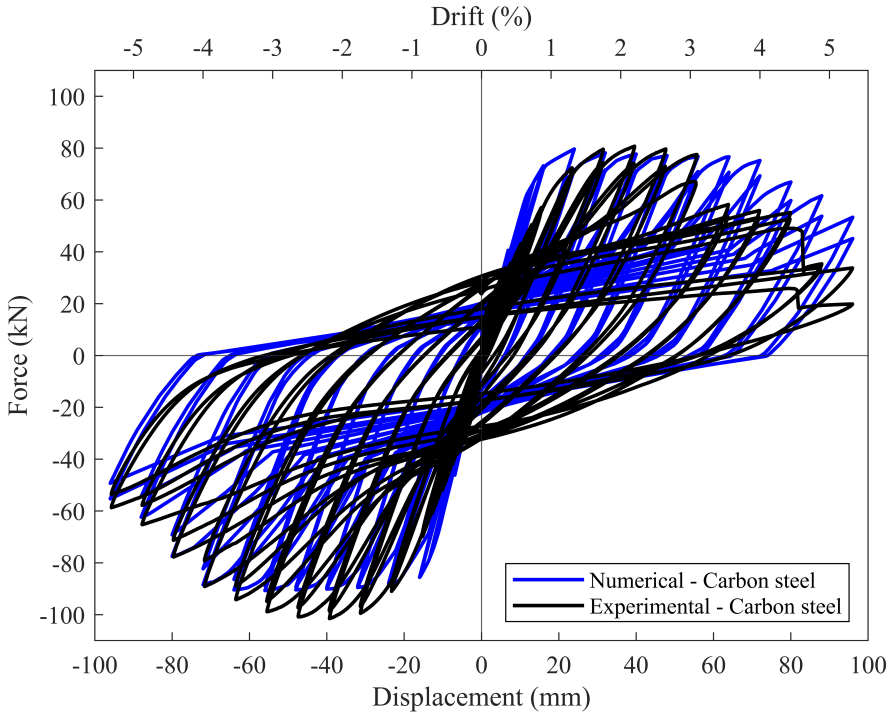

Figure 18: Numerical and experimental lateral force-drift comparisons for carbon steel column including damage1.

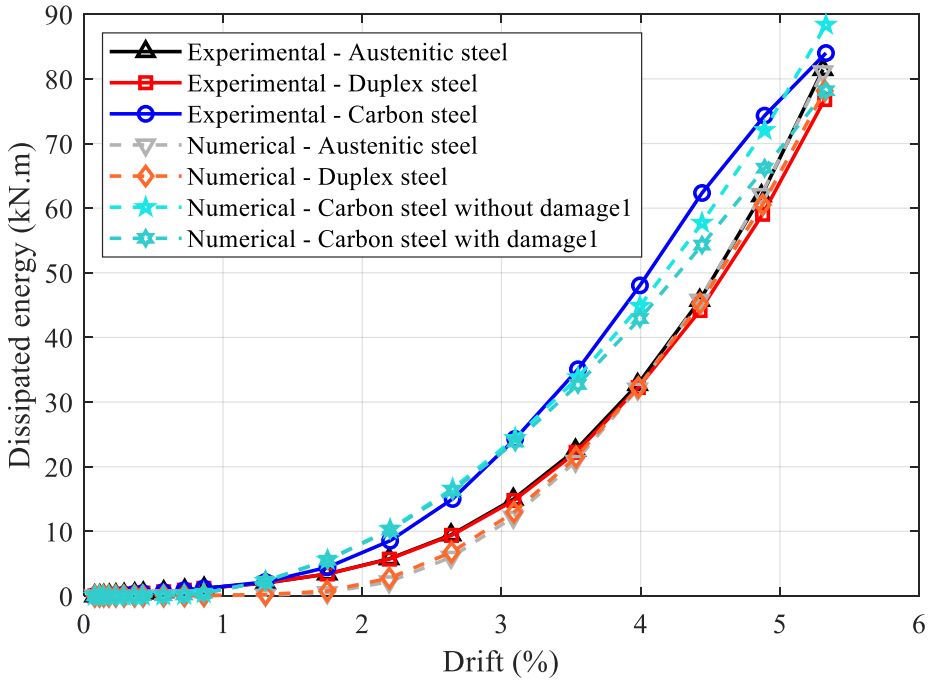

Figure 19: Comparison of the experimental and numerical hysteretic dissipated energy evolutions.

Tables

Table 1: Measured tensile mechanical properties of the reinforcing bars.

Rebar	E (MPa)	$f_{0.2}$ (MPa)	f_u (MPa)	ε_u (%)	ε_f (%)	n	$n'_{0.2,u}$
EN 1.4301- 8mm (CR)	191000	735	886	5.1	16.6	4.7	14.7
EN 1.4301- 16mm	192000	764	952	17.6	29.4	6.4	3.9
EN 1.4362- 8 mm (HR)	175000	608	802	19.7	32.0	5.6	5.8
EN 1.4362- 16 mm	183000	539	766	21.2	32.1	5.1	4.3
B500 (A) - 8mm (CR)	200426	520	645	5.7	15.2	-	-
B500 (C) - 16mm (HR)	193913	530	640	16.5	22.7	-	-

Table 2: Cameras, settings and parameters used in digital image correlation.

Stereo DIC		
Column Side	Positive loading direction side	Negative loading direction side
Camera		
Sensor & digitization	CCD 2456×2058 pixels, 8-bit	CCD 2456×2058 pixels, 8-bit
Exposure time & recording rate	19000 μs, 1 Hz	19000 μs, 1 Hz
Mean camera noise (% of dynamic range)	0.0041% (left camera); 0.0039% (right camera)	0.0037% (left camera); 0.0034% (right camera)
Lens & imaging distance	Nikkor 50 mm, 2.69 m	Nikkor 28 mm, 1.55 m
Number of images averaged for resolution calculation	2	2
Pixel size	3.45 μm	3.45 μm
Region of interest & field of view	100×200 mm, 442×370 mm	100×200 mm, 537×450 mm
Processing		
Subset, step	59, 16 pixels	59, 16 pixels
Matching criterion, interpolation, shape function	ZNSSD, Local Bicubic Spline, Quadratic	ZNSSD, Local Bicubic Spline, Quadratic
Pre-smoothing	None	None
Mean displacement resolution	0.0508 mm [1.06 pixels]	0.0383 mm [1.18 pixels]
Strain		
Smoothing technique	None	None
Virtual strain gauge	7 pixels (24.15 μm)	7 pixels (24.15 μm)
Mean strain resolution	533 με	524 με

Table 3: Summary of the measured force and drift values for the positive loading direction.

Column specimen	$F_{c,max}$ (kN)	$\delta_{c,max}$ (%)	δ_y (%)	$F_{c,ult}$ (kN)	$\delta_{c,ult}$ (%)	$\mu_{\Delta,ult}$
Austenitic EN 1.4301	125.75	3.53	1.94	117.95	5.31	2.74
Duplex EN 1.4362	88.28	3.09	1.76	79.53	5.32	3.02
Carbon steel B500 (C)	80.76	2.20	1.22	64.61	3.40	2.79

Table 4: Summary of measured force and drift values for the negative loading direction.

Column specimen	$F_{c,max}$ (kN)	$\delta_{c,max}$ (%)	δ_y (%)	$F_{c,ult}$ (kN)	$\delta_{c,ult}$ (%)	$\mu_{\Delta,ult}$
Austenitic EN 1.4301	115.4	3.07	1.82	103.7	5.31	2.92
Duplex EN 1.4362	99.57	2.63	1.56	84.69	5.31	3.40
Carbon steel B500(C)	101.5	2.20	1.26	81.21	4.29	3.40

Table 5: *Concrete02* (unconfined) and *Concrete04* (confined) material model parameters.

Column	Concrete	f_c (MPa)	ε_0 (‰)	ε_{cu} (‰)	f_{tu} (MPa)
Carbon steel column	Unconfined	60.3	2.6	10.0	4.4
	Confined	70.9	4.9	22.0	4.4
Austenitic stainless steel column	Unconfined	52.1	2.5	10.0	4.1
	Confined	66.9	5.9	33.5	4.1
Duplex stainless steel column	Unconfined	51.9	2.5	10.0	4.1
	Confined	64.2	5.4	28.5	4.1

Table 6: *Hysteretic* material model parameters for reinforcing bar fibres

Specimen/ model parameter	Carbon steel column	Austenitic stainless steel column	Duplex stainless steel column
σ_1 (MPa)	530	764	539
ε_1 (%)	0.27	0.62	0.53
σ_2 (MPa)	640	844	619
ε_2 (%)	16.48	1.01	1.01
σ_3 (MPa)	429	952	766
ε_3 (%)	22.74	17.60	21.24
β_{MU} (-)	0.40	0.35	0.10
PinchX	0.4	0.4	0.5
PinchY	0.4	0.5	0.8
Damage1	0.008	0	0

Table 7: Comparison of the maximum force $F_{c,max}$ and displacement at maximum force $\delta_{c,max}$ in the positive (+) and negative (-) loading directions of the experimental and numerical column responses.

		Austenitic stainless steel	Duplex stainless steel	Carbon steel without damage 1	Carbon steel with damage1
$F_{c,max}$ (+)	Experimental (kN)	125.75	88.28	80.76	80.76
	Numerical (kN)	126.50	87.12	79.65	79.65
	Experimental/numerical	0.995	1.01	1.01	1.01
$\delta_{c,max}$ (+)	Experimental (mm)	63.54	55.58	39.57	39.57
	Numerical (mm)	48.00	40.00	24.00	24.00
	Experimental/numerical	1.32	1.38	1.64	1.64
$F_{c,max}$ (-)	Experimental (kN)	115.45	99.57	101.51	101.51
	Numerical (kN)	109.34	86.12	90.92	90.68
	Experimental/numerical	1.056	1.156	1.116	1.194
$\delta_{c,max}$ (-)	Experimental (mm)	55.21	47.29	39.31	39.31
	Numerical (mm)	40.00	62.01	63.00	56.00
	Experimental/numerical	1.380	0.762	0.624	0.702